ACS APPLIED MATERIALS & INTERFACES

www.acsami.org Research Article

Nanopore-Patterned CuSe Drives the Realization of the PbSe−CuSe Lateral Heterostructure

Bo Li, Jing Wang, Qilong Wu, Qiwei Tian, Ping Li,* Li Zhang, Long-Jing Yin, Yuan Tian, Ping Kwan Johnny Wong, Zhihui Qin,* and Lijie Zhang*

Cite This: *ACS Appl. Mater. Interfaces* 2022, 14, 32738−32746 Read Online

ABSTRACT: Monolayer PbSe has been predicted to be a two-dimensional (2D) topological crystalline insulator (TCI) with crystalline symmetry-protected Dirac-cone-like edge states. Recently, few-layered epitaxial PbSe has been grown on the $SrTiO_3$ substrate successfully, but the corresponding signature of the TCI was only observed for films not thinner than seven monolayers, largely due to interfacial strain. Here, we demonstrate a two-step method based on molecular beam epitaxy for the growth of the PbSe−CuSe lateral heterostructure on the Cu(111) substrate, in which we observe a nanopore-patterned CuSe layer that acts as the template for lateral epitaxial growth of PbSe. This further results in a PbSe−CuSe lateral heterostructure with an atomically sharp interface. Scanning tunneling microscopy and spectroscopy measurements reveal a fourfold symmetric square lattice of such PbSe with a quasi-particle band gap of 1.8 eV, a value highly comparable with the theoretical value of freestanding PbSe. The weak monolayer−substrate interaction is further supported by both density functional theory (DFT) and projected crystal orbital Hamilton population, with the former predicting the monolayer's anti-bond state to reside below the Fermi level. Our work demonstrates a practical strategy to fabricate a high-quality in-plane heterostructure, involving a monolayer TCI, which is viable for further exploration of the topology-derived quantum physics and phenomena in the monolayer limit.

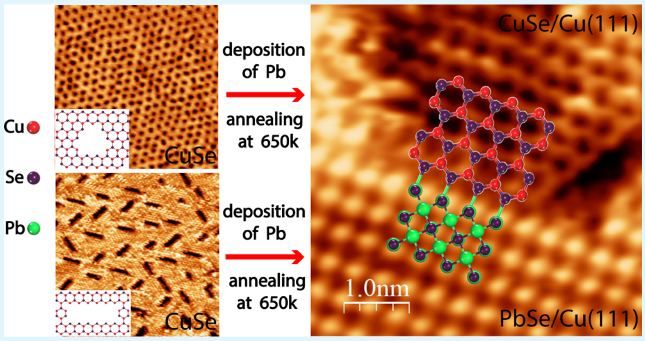

KEYWORDS: *PbSe, CuSe, scanning tunneling microscopy/spectroscopy, lateral heteroepitaxy, two-dimensional topological crystalline insulator*

■ INTRODUCTION

To date, various kinds of monolayer two-dimensional (2D) materials, such as graphene and transition metal dichalcogenides (TMDs), can be physically or chemically isolated from their parent crystals. Being in the monolayer limit, these 2D materials often exhibit richer properties that are not found in their 3D forms.[1] The 2D topological insulating phase is one such exotic state of matter known for elemental 2D materials such as silicene,[2−7] germanene,[8−13] stanene,[14−16] and bismuthene,[17] in which the theoretically predicted quantum spin Hall effect may be explored at experimentally accessible temperatures.[18−21] In addition, the substrate effect is crucial to the topological properties.[22] On the other hand, the synthesis of the binary honeycomb structure of Sn_2Bi provides a platform for the studies of strongly correlated phenomena.[23] Along with other members of group IV-VI components that are best known for applications in thermoelectrics, optoelectronics, and spintronics,[24−27] PbSe is a narrow gap semiconductor crystallized in a rock salt structure. Remarkably, recent theory has predicted PbSe to possess a 2D topological crystalline insulator (TCI) phase when its physical dimension is reduced to monolayer.[28] While a vigorous proof of such a 2D TCI phase is yet to be seen, possible signature has been reported for epitaxial PbSe with seven layers grown on $SrTiO_3$ substrate. Lowering the layer number further for the search of the 2D TCI is, however, limited by interface strain that breaks the crystal symmetry of PbSe. To this end, achieving strain-free PbSe is vital.

Here, we demonstrate the synthesis of PbSe−CuSe lateral heterostructure on Cu(111) by means of two-step molecular beam epitaxy, in which a nanopore-patterned CuSe layer has been employed as the template for lateral epitaxy of PbSe, thereby forming a PbSe−CuSe lateral heterostructure. Scanning tunneling microscopy (STM) measurements show that the synthesized PbSe exhibits a fourfold symmetry with a periodicity of 0.43 nm. A quasi-particle band gap of 1.8 eV has been

Received: May 11, 2022
Accepted: June 27, 2022
Published: July 8, 2022

https://doi.org/10.1021/acsami.2c08397
ACS Appl. Mater. Interfaces 2022, 14, 32738−32746

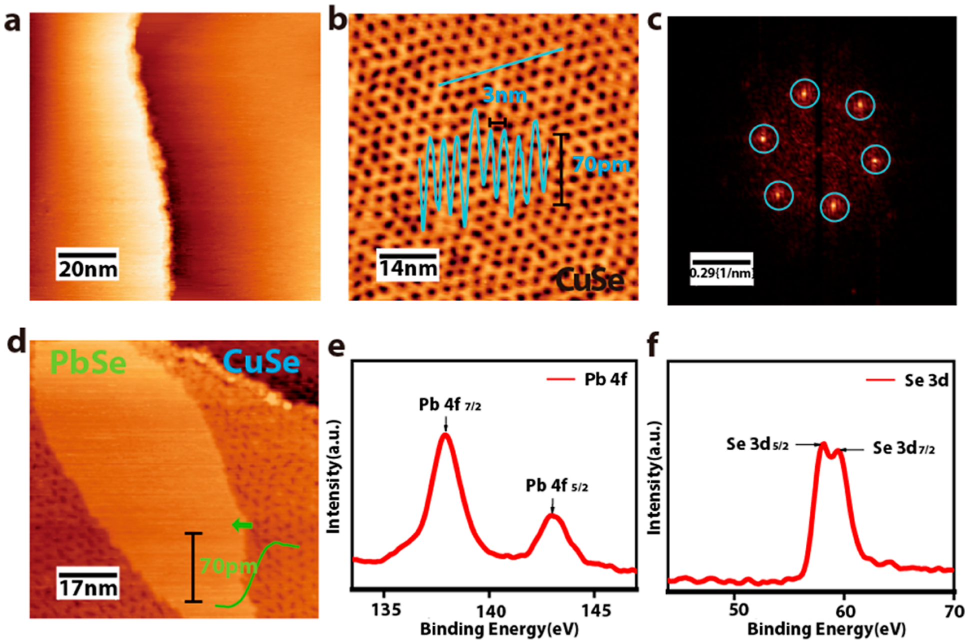

Figure 1. Realization of PbSe−CuSe lateral heterostructure. (a) Large-scale STM image of clean Cu(111) substrate. Sample bias is 0.5 V and tunnel current is 80 pA. (b) Typical STM topographic image of CuSe with intrinsic triangular nanopores on Cu(111) substrate. An inset line profile reveals that the periodicity of nanopores pattern is ∼3 nm, and the depth of the nanopores is ∼70 pm (V = 1.4 V, I = 80 pA). (c) 2D fast Fourier transform (FFT) pattern made from (b). The bright dots marked by cyan circles confirm the hexagonal periodicity of the nanopores. (d) STM topographic image of PbSe surrounded by CuSe. The inset height profile shows that the step height of the film is ∼70 pm (V = 1 V, I = 90 pA). (e,f) XPS spectra of the Se 3d and Pb 4f core levels, respectively.

obtained by scanning tunneling spectroscopy (STS), revealing no major hybridization between PbSe and Cu(111) substrate. Our experimental results are in line with density functional theory (DFT) and projected crystal orbital Hamilton population (pCOHP), confirming a band gap of ∼1.5 eV for freestanding PbSe and weak monolayer−substrate interaction.

■ RESULTS AND DISCUSSION

Figure 1a shows a typical STM topographic image of large-scale Cu(111) substrate. After the deposition of a sub-monolayer (ML) of Se atoms and subsequent annealing at ∼650 K for 10 min, monolayer CuSe decorated with patterned nanopores is formed (Figure 1b). Previous reports indicated that the nanopores are related to Se-concentration and originated from the lattice mismatch between CuSe and Cu(111) substrate.[29−31] In accordance with the previous findings,[29] these triangular nanopores exhibit a hexagonal structure with a periodicity of ∼3 nm and a depth of ∼70 pm, as confirmed by the line profile in Figure 1b. Figure 1c shows a fast Fourier transform (FFT) of Figure 1b, revealing a hexagonal periodicity of the nanopores. It is worth mentioning that the nanopores exhibit not only triangular but also parallelogram shapes. The morphology of CuSe shown in Supporting Information Figure S1 further reveals the zigzag edges of the nanopores. To form PbSe, Pb atoms were evaporated to the surface in ultrahigh vacuum. Subsequent annealing at ∼650 K for 10 min leads to the formation of a thin film island (Figure 1d). It is seen that the island possesses an apparent height of only 70 pm, much less than one atomic layer thickness of PbSe. This height difference strongly suggests the formation of PbSe atop Cu(111), instead of directly on CuSe, thus forming a lateral heterostructure with CuSe, which is schematically depicted in Figure S2 in the Supporting Information. We will elaborate this in more detail in latter section. X-ray photoelectron spectroscopy (XPS) was conducted to verify the valence states of Pb and Se ions. Figure 1e shows the main peaks at 137.9 and 142.9 eV corresponding to $Pb4f_{7/2}$ and $Pb4f_{5/2}$, respectively, of PbSe.[32] Similarly, Figure 1f indicates the two Se3d peaks at 54.05 and 54.7 eV due to PbSe and CuSe.

To gain more information of the surface, we investigated the structural and electronic properties of PbSe and the surrounding CuSe. Figure 2a shows an atomic resolution STM image of PbSe. Clearly, the PbSe exhibits a fourfold symmetric square lattice, with its FFT shown in the inset of Figure 2a. The proposed top and side view of the PbSe ball−stick model is shown in Figure 2b. In order to determine the structure of PbSe on Cu(111), we investigated the thermodynamic stability of single atom layer (space group $P4/mmm$) and double atom layer (space group $P4/nmm$) PbSe, as shown in Figure S3. For the $P4/mmm$ PbSe, it has relatively large imaginary frequency, implying its low stability, while for the $P4/nmm$ PbSe, its imaginary frequency almost disappears. Note that the small imaginary frequencies near the Γ point are probably due to the numerical errors. Hence, we consider the $P4/nmm$ PbSe to be dynamically stable. As such, it is the $P4/nmm$, rather than $P4/mmm$, PbSe monolayer, that formed on the Cu(111) substrate, with two sublayers.[33] In Figure 2a, we obtain a structural periodicity of 0.43 nm and thus the lattice constant of the synthesized PbSe. In order to know which atoms are resolved by STM, we simulated the STM image, as shown in Figure S4, and found that only Pb atoms were visible under the empty state, which might be due to the higher surface height of Pb than Se atoms. This finding is similar to the cases of PbTe and γ-SnTe, where only Pb and Sn atoms can be resolved by STM.[34,35] In a previous study of few-layered PbSe grown on $SrTiO_3$, the authors observed considerable compressive strain due to the mismatch between PbSe and the substrate.[36] Here, on the contrary, we have not found any strain effect, even though PbSe and Cu(111) are not

https://doi.org/10.1021/acsami.2c08397
ACS Appl. Mater. Interfaces 2022, 14, 32738−32746

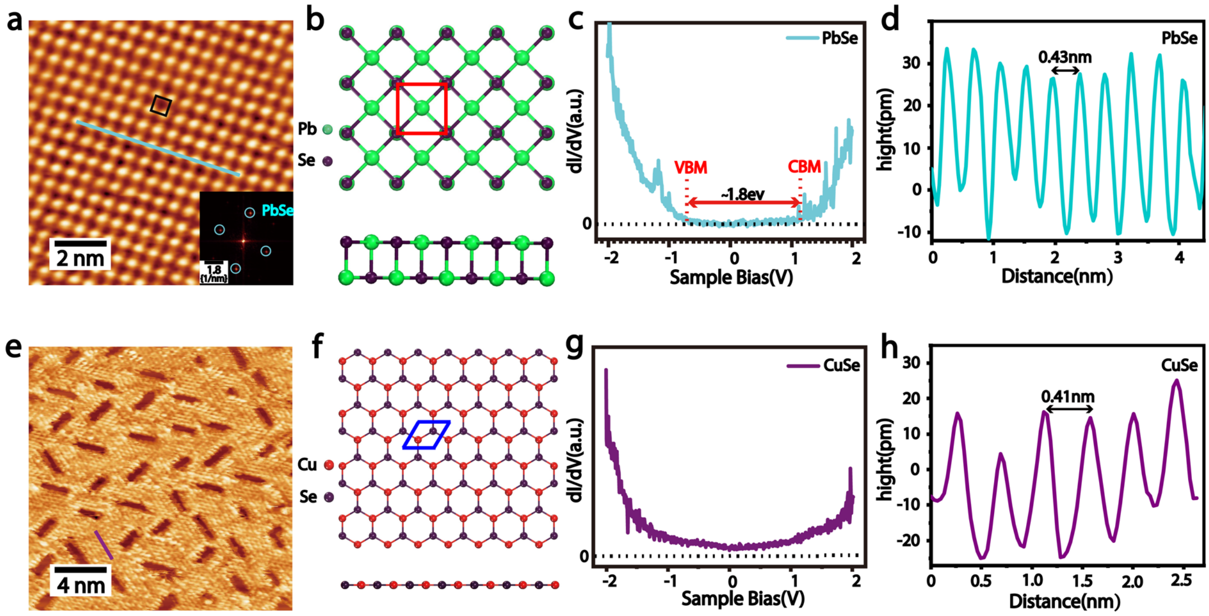

Figure 2. Characteristic of PbSe and CuSe. (a) High-resolution STM images of PbSe ($V = -500$ mV, $I = 90$ pA). Inset: the corresponding FFT pattern with the cyan circles marked the reciprocal lattice peaks of PbSe. (b) Ball and stick model of PbSe crystalline structure (upper panel: top view, lower panel: side view). (c) dI/dV spectra of PbSe, revealing a band gap of ∼1.8 eV. (d) Line profile of PbSe along the line marked in (a), revealing the periodicity of the synthesized PbSe is ∼0.43 nm. (e) High-resolution STM images of monolayer CuSe ($V = 1$ V, $I = 90$ pA). (f) Ball and stick model of CuSe crystalline structure (upper panel: top view, lower panel: side view). (g) dI/dV spectra of monolayer CuSe, revealing a clear metallic property. (h) Line profile of CuSe along the line marked in (e), revealing the periodicity of CuSe is ∼0.41 nm.

structurally matched. For instance, the structure of Cu(111) is hexagonal with a threefold symmetry, whereas PbSe exhibits a fourfold symmetric square structure. The incommensurate epitaxy involved here reduces the PbSe−substrate interaction, which also explains the absence of strain-induced lattice constant variation in our PbSe film. The resulting quasi-freestanding nature of the monolayer has also been verified by the dI/dV spectrum in Figure 2c. One can see that the valance band maximum (VBM) and conductance band minimum (CBM) are located at −0.65 and 1.15 eV, respectively, thus giving a quasi-particle band gap of 1.8 eV. Our measured large band gap reveals that no hybridization occurs between PbSe and Cu(111) substrate.[37] An atomic resolution STM image of CuSe around PbSe is shown in Figure 2e. The parallelogram nanopores distribute on the surface with varied orientations. A ball and stick model has been shown in Figure 2f, constructed based on the observation of CuSe structure, in accordance with a previous report.[29] A line profile in Figure 2h along the line marked in Figure 2e shows that the periodicity of CuSe is ∼0.41 nm, fitting quite well with the previous report.[29] The differential conductance spectrum in Figure 2g further indicates a metallic character of the CuSe layer. To gain more information of the formation mechanism of PbSe, we have scrutinized the growth procedure. We increased the concentration of Se to more than 1 ML on Cu(111) to obtain CuSe without nanopore pattern.[30,31] Figure 3a shows a large-scale STM image of nanopore-free CuSe. A zoom-in atomic resolution STM image shown in Figure 3b reveals the same lattice parameters (see the inset in Figure 3b of ∼0.41 nm) of nanopore-free CuSe and patterned one. Figure 3c shows an STM image of the surface after the deposition of Pb atoms. The marked bright protrusions are Pb clusters prior to annealing. Upon annealing at ∼650 K for 10 min, the adsorbed Pb clusters disperse to Pb adatoms rather than forming a PbSe/CuSe heterostructure (see in Figure 3d). The failed formation of PbSe suggests the crucial role of the nanopore-patterned CuSe.

Nevertheless, as mentioned before, the nanopore-patterned CuSe could be realized by deposition of sub-ML Se on Cu(111), as also shown in Figure 3e. As mentioned before, there are two types of the nanopores of the patterned CuSe. They are visible in the two regions in Figure 3e labeled as I and II to distinguish them. Afterward, we deposited Pb atoms on the patterned CuSe surface. Obviously, bright protrusions of Pb adatoms/clusters are visible and are distributed randomly on the nanopore-patterned CuSe surface, as shown in Figure 3f. Subsequent annealing leads to the co-existence of PbSe and CuSe (see Figure 3g). Figure 3h,i shows the formed PbSe/CuSe in-plane heterostructure with two types of interfaces labeled as I′ and II′, which correspond to the type I and II nanopores. Figure 3j,k illustrates the proposed schematic model for the formation mechanism of PbSe−CuSe lateral heterostructure. Two types of intrinsic nanopores decorated CuSe are schematically shown in Figure 3j, corresponding to that in Figure 3e. The nanopores expose dangling bonds that form local nucleation sites for PbSe, whereas the nanopore-free terraces of CuSe are fully saturated, thus preventing the nucleation. Furthermore, the interaction of the substrate might also take a role of preventing the nucleation. We proposed a mechanism of lateral heteroepitaxy PbSe templated by patterned CuSe as shown in Figure 3k. The Se atoms at the side of CuSe are bonded with Pb to achieve an epitaxy with PbSe and the growth is boosted to the other three directions (see the marked arrows in Figure 3k). As such, we explicitly conclude that the formation of PbSe−CuSe lateral heterostructure is related to nanopore-patterned CuSe.

In order to further confirm the formation mechanism of PbSe−CuSe lateral heterostructure, we focus on the structural and electronic properties of the interface. Figure 4a shows a large-scale STM image of the PbSe−CuSe lateral heterostructure on the Cu(111) substrate. Figure 4b shows an atomic resolution STM image simultaneously resolved with atomic resolution of PbSe and CuSe. Clearly, PbSe exhibits a square

https://doi.org/10.1021/acsami.2c08397
ACS Appl. Mater. Interfaces 2022, 14, 32738−32746

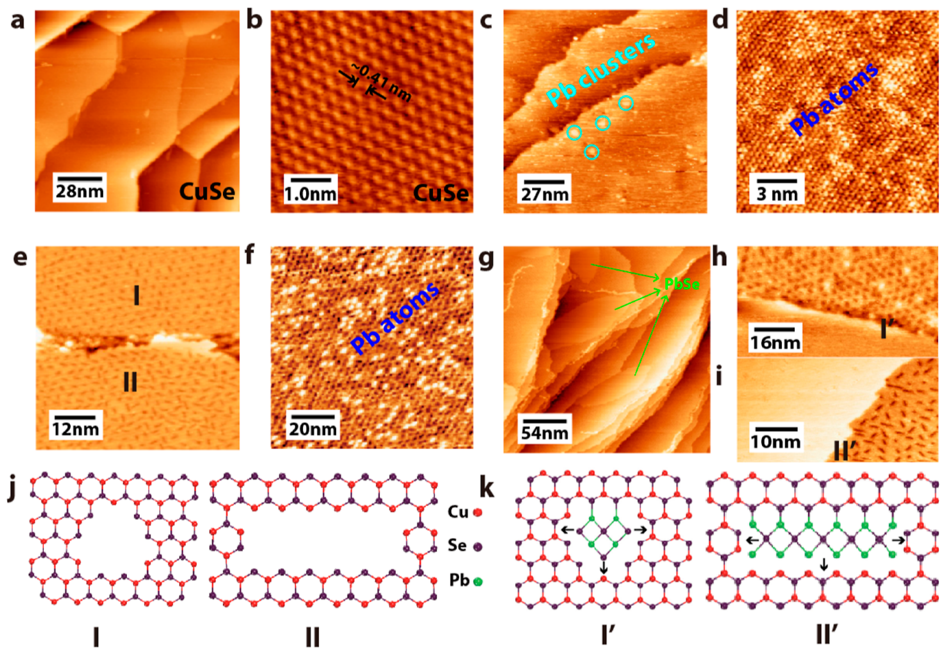

Figure 3. Formation route of PbSe. (a) Large-scale STM image of CuSe without nanopores ($V = 2$ V, $I = 10$ pA). (b) Atomic resolution STM image of CuSe without nanopores on the Cu(111) substrate ($V = 1$ V, $I = 90$ pA). (c) Large-scale STM topographic image of Pb evaporated on a nanopore-free CuSe ($V = 1$ V, $I = 100$ pA). The marked bright protrusions are Pb clusters. (d) STM topography after annealing of (b) ($V = 1$ V, $I = 90$ pA). The bright dots are Pt atoms. (e) Large-scale STM image of the CuSe with two types of nanopores on the Cu(111) substrate ($V = 1.3$ V, $I = 59$ pA). Type I: triangle shape, and Type II: parallelogram shape. (f) STM topography of Pb evaporated on CuSe with nanopores ($V = 1$ V, $I = 90$ pA). The bright protrusions are Pb clusters. (g) Large-scale STM topographic image of PbSe islands surrounded by CuSe ($V = 1$ V, $I = 90$ pA). (h,i) STM images of PbSe/CuSe in-plane heterostructures based on two types of nanopores as shown in (e), labeled as I′ and II′, respectively ($V = 1$ V, $I = 90$ pA). (g) STM topography of the PbSe−CuSe lateral heterostructure obtained by annealing (e) ($V = 700$ mV, $I = 90$ pA). (j) Ball and stick models for nanopores CuSe. Type I and II are triangle and parallelogram, respectively, corresponding to the STM image in (e). (k) Schematic diagram of the formation of PbSe/CuSe heterostructure. The left panel labeled by I′ corresponds to I, whereas the right panel II′ to II. The arrows are the growth direction of PbSe.

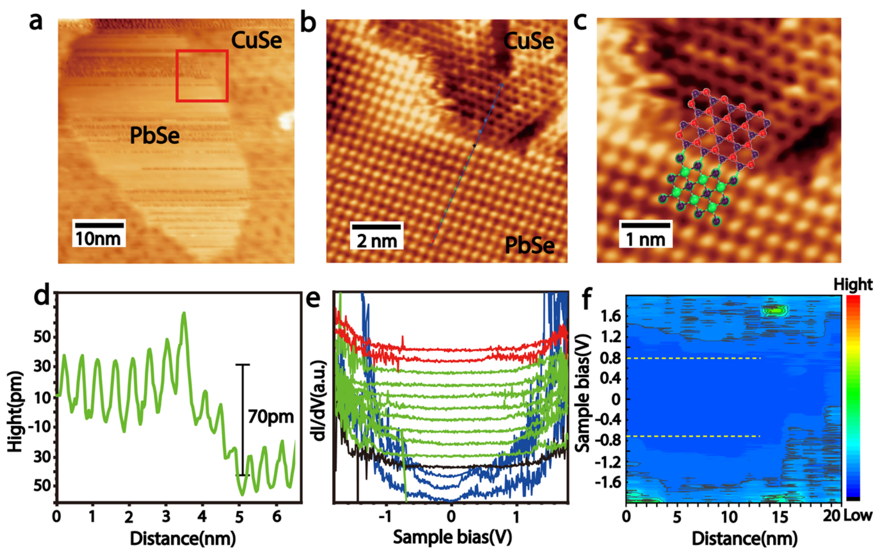

Figure 4. Electronic properties of the PbSe−CuSe lateral heterostructure. (a) Large-scale STM image of the PbSe and CuSe on the Cu(111) substrate ($V = 1.4$ V, $I = 40$ pA). (b) Atomic resolution STM image of PbSe and CuSe on the Cu(111) substrate ($V = -500$ mV, $I = 90$ pA). (c) Zoom-in STM image of the interface of PbSe and CuSe. Ball and stick model on top to reveal the structural properties of the interface bounding. (d) Line profile along the green line marked in (b) shows the step height of ∼70 pm. (e) Serials dI/dV spectra collected from PbSe to CuSe crosses the step edge, showing the electronic properties of PbSe and CuSe. (f) Color mapping of the real-space imaging of the band profile plotted in terms of the dI/dV.

lattice, whereas CuSe exhibits a honeycomb one. A zoom-in STM image of the interface is shown in Figure 4c, indicating that the two sides are connected with each other by means of an atomic sharp interface, indicating the lateral heteroepitaxial growth of PbSe based on CuSe. It is comparable to the previous report of hBN and graphene,[38] whereas the difference between the two cases is that the requirement of consummation of nanopore-patterned CuSe to grown PbSe. As seen in the proposed schematic aforementioned in Figure 3k, we find the interface boundary consisted of Se bond with Pb atoms (see also

https://doi.org/10.1021/acsami.2c08397
ACS Appl. Mater. Interfaces 2022, 14, 32738−32746

the highlighted ball and stick model inset of Figure 4c). It indicates that our proposal model fit quite well with the experimental observations, revealing the lateral heterostructure formed this way. It also explains the measured height of the PbSe islands of only ~70 pm (see Figure 4d), far from one atom thick. In addition, the interface interaction between PbSe and Cu(111) is weak as discussed before. Lateral heterostructures based on 2D materials have received extensive attention in recent years.[39−44] Among them, graphene-hBN and TMD-based lateral heterostructures are the most extensively studied ones.[45,46] Heteroepitaxial growth of hBN templated by graphene edges opened pathways for construction of the hBN-graphene lateral heterostructure with the atomic clean lateral interface.[38] Recently, these lateral heterostructures have expanded to other systems, for instance, borophene-graphene and borophene-hBN lateral heterostructures.[47,48] Here, in our case, we expand the strategy further. The nucleation occurs inside the nanopores of the patterned CuSe. By templating the nanopore-patterned CuSe, PbSe grows laterally [follow the arrows marked in other three directions (see Figure 3k)] by dissociation of CuSe. Therefore, PbSe islands would form and are surrounded by CuSe, which is in line with our experimental observations. We calculated the formation energy by $E_f = (E_{tot} - N_{Cu}\mu_{Cu}/N_{Pb}\mu_{Pb} - N_{Se}\mu_{Se})/N_{tot}$, and the obtained formation energy values of CuSe and PbSe are −3.48 and −4.20 eV, respectively. It is noted that the formation energy of PbSe is lower than CuSe, revealing the easier formation of PbSe. We conducted the differential conductance; follow the line marked in the inset of Figure 4b. The series dI/dV spectra verify the transition from semi-conducting to metallic properties from PbSe to CuSe. Room temperature induced noise of the dI/dV spectra mainly in the high energy zone, which would not influence the characteristics in the vicinity of the Fermi level. Figure 4f shows a color mapping of the real space based on the series dI/dV spectra spatially obtained from the surface, where we clearly find the band structure transition of PbSe to CuSe. We continued depositing Pb on PbSe to check its absorption and found that the Pb atoms are absorbed on the edges of PbSe islands rather than on top of PbSe (see Figure S5 in the Supporting Information). Subsequent annealing leads to the expansion of PbSe islands rather than forming the second layer of PbSe. Therefore, we further verify the monolayer feature of PbSe.

To support our observation in experiments, we performed the first-principles calculations based on DFT. We have performed an extensive search for the stable structure of CuSe/Cu(111) and PbSe/Cu(111). We notice that the $\sqrt{3} \times \sqrt{3}$ ($\sqrt{10 \times 1}$) unit cell of CuSe (PbSe) is commensurate to the $\sqrt{7} \times \sqrt{7}$ ($2\sqrt{7} \times \sqrt{3}$) Cu(111) with a lattice mismatch of less than 5%. We have considered three typical configurations (see Figure S6 in the Supporting Information); the Pb/Cu atom is on the top, bridge, and hollow positions of the quadrilateral formed by the top layer Cu atoms, respectively. After extensive geometry optimizations, we found that the bridge CuSe/Cu(111) and hollow PbSe/Cu(111) structures are the most stable structures. For the CuSe/Cu(111) heterostructure, the top structure is more consistent with the experimentally grown structure. Hence, we take top CuSe/Cu(111) and hollow PbSe/Cu(111) as the objects for the following investigation.

To quantify the interaction between CuSe/PbSe and Cu(111) substrate, we calculated the binding energy E_b, which is defined as $E_b = (E_{CuSe/PbSe} + E_{Cu(111)} - E_{tot})/N$. $E_{CuSe/PbSe}$, $E_{Cu(111)}$, and E_{tot} are the total energies of the CuSe/PbSe, the Cu(111) substrate, and the total energies of the CuSe/Cu(111) or PbSe/Cu(111), and N is the number of the CuSe/PbSe atoms at the interface. The calculated E_b is shown in Table 1.

Table 1. Binding Energy E_b (eV/Atom) of the Three Structures for CuSe and PbSe on the Cu(111) Substrate

	bridge (eV)	hollow (eV)	top (eV)
CuSe	1.12	1.12	0.87
PbSe	0.62	0.62	0.61

The binding energy of CuSe is almost twice that of PbSe. It indicates that the interfacial interaction between PbSe and Cu(111) is much weaker than that between CuSe and Cu(111). In addition, the binding energies (0.61−0.62 eV/atom) are comparable to that of CrI3 on BiFeO3 semiconductor substrate: 0.28−0.41 eV/Cr and 0.34−0.51 eV/I,[49] indicating the nature of vdW interaction between PbSe and Cu(111).

Figure 5 illustrates the total density of states (TDOS) of CuSe and PbSe with/without the Cu(111) substrate. We find that the CuSe film is metallic regardless of whether the substrate stays there or not. However, the situation of PbSe case is completely different. When the substrate is there, the heterostructure shows metallic property because the electronic state of the metal Cu(111) substrate is included, whereas it shows semiconducting property without the substrate. Figure 5b shows the TDOS of freestanding PbSe without the Cu(111) substrate by HSE06 functional, showing a band gap of ~1.5 eV, which is, actually, in accordance with our experimental measurements. It indicates the weak interaction between PbSe and Cu(111) substrate, which is consistent with our experimental observations.

In order to systematically understand the physical mechanism, the synthesized semiconducting PbSe is weakly coupled from the substrate, and we identified chemically bonded atom pairs via electron localization function (ELF) analysis. It can be a good substitute for the ambiguous distance cutoff method commonly used in a previous work.[50] It is defined as ELF = $1/[1 + (D/D_h)]$, where $D = \frac{1}{2}\sum_i |\nabla\varphi_i|^2 - \frac{1}{8}\frac{|\nabla\rho|^2}{\rho}$ and $D_h = \frac{3}{10}(3\pi^2\rho)^{5/3}$. The φ_i denotes the Kohn−Sham orbitals and $\rho = \sum_i |\varphi_i|^2$ represents the electron charge density. The ELF provides a value between 0 and 1. ELF = 0.5 stands for the same level of Pauli repulsion as in the homogeneous electron gas, while a higher ELF value signifies that the electrons are more localized (ELF = 1 indicates perfect localization of electrons). Figure S7 in the Supporting Information shows the ELF for CuSe/Cu(111) and PbSe/Cu(111), which is a typical nearly free electron state at the interface. We found that the values of ELF between CuSe, PbSe layer, and the Cu(111) substrate are lower than 0.5, indicating a weak interfacial interaction. In order to quantify and compare the strength of the interface interaction between CuSe and Cu(111) and between PbSe and Cu(111), we introduced pCOHP to analyze the interface interaction. We follow the usual way of displaying -pCOHP, namely, the positive values of -pCOHP indicate the bonding states, while negative values denote the antibonding states. For CuSe/Cu(111) (Figure 6a) and PbSe/Cu(111) (Figure 6b), the interface has antibonding states within $E \sim E_F - 2.5$ and $E \sim E_F - 2.0$ eV (in the valence bands), indicating that the interface interaction is weaker. In order to better demonstrate the COHP results, the ipCOHP is defined as follows: $-\text{ipCOHP} = \int_{-\infty}^{E_F} -\text{pCOHP}dE$, −ipCOHP indicates the extent of interface interaction strength.

https://doi.org/10.1021/acsami.2c08397
ACS Appl. Mater. Interfaces 2022, 14, 32738−32746

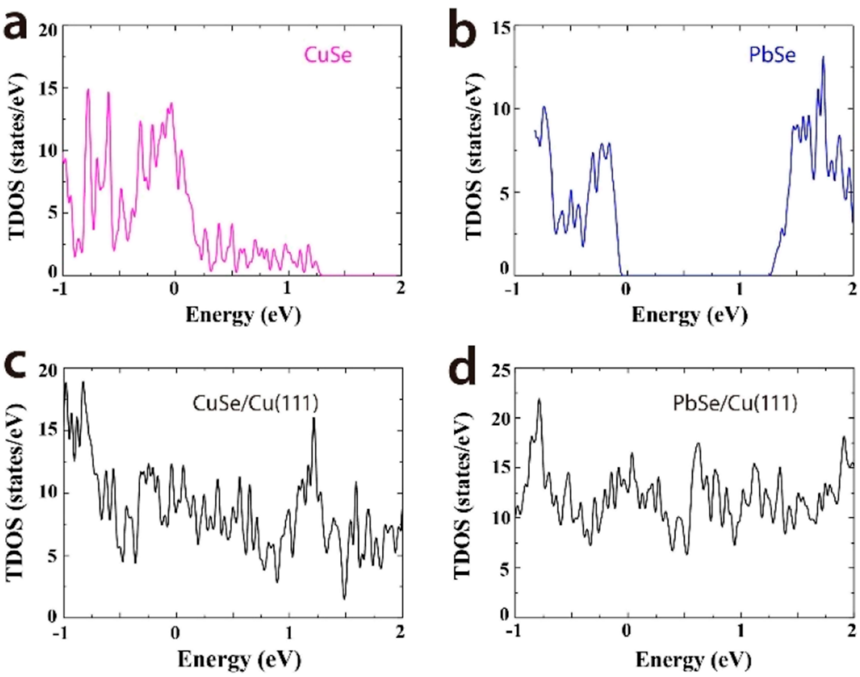

Figure 5. Total density of states (TDOS) of CuSe and PbSe. (a) TDOS of CuSe detached from Cu(111). (b) TDOS of PbSe detached from Cu(111) by HSE06 functional. (c,d) TDOS of CuSe/Cu(111) and PbSe/Cu(111), respectively. Zero refers to the Fermi level.

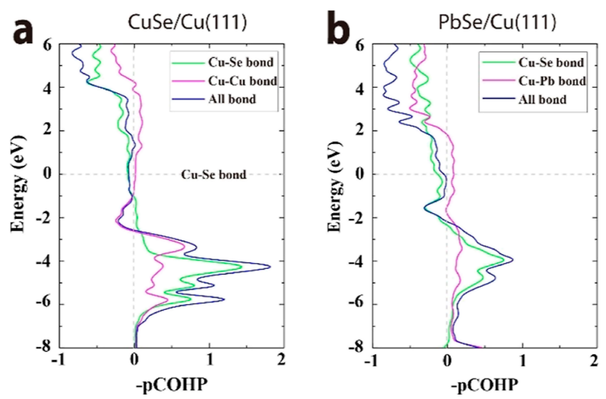

Figure 6. Interaction comparison between the overlayer and the substrate. Plane wave pCOHP between Cu and Cu, Se atoms (a) and between Cu and Pb, Se atoms (b) at the interface. −pCOHP > 0 denotes the bonding state, while −pCOHP < 0 indicates the antibonding state. Energy is shifted, so that the Fermi level E_F equals zero.

The value of −ipCOHP is smaller, indicating the weaker interface interaction. The −ipCOHP values for CuSe/Cu(111) and PbSe/Cu(111) are 5.06 and 1.54, respectively. It indicates that the interface interaction of the PbSe/Cu(111) is much weaker than that of CuSe/Cu(111). It well explains why the dI/dV spectrum of PbSe/Cu(111) experimentally shows semiconducting property. Moreover, in order to confirm the weak van der Waals (vdW) between PbSe and Cu(111) substrate, we calculated and compared the effect of the substrate on the band structures. As shown in Figure S8, we found that the Cu(111) substrate has little effect on the band structure. It indicates that there is a weak vdW interaction between PbSe and Cu(111) substrate, which can be ignored. It provides a platform to detect topological properties for the next step.

■ CONCLUSIONS

In summary, we have successfully synthesized a PbSe−CuSe lateral heterostructure by sequential deposition of Se and Pb on Cu(111). We find that nanopore-patterned CuSe acts as a template for lateral epitaxy of PbSe, forming a PbSe−CuSe lateral heterostructure. STM and STS show the structural and electronic properties of PbSe, confirming that its fourfold symmetry directly locate on Cu(111) through a weak interaction. The detailed atomic lattice of the obtained PbSe shows a lattice constant of 0.43 nm, revealing no strain effect exist. By combining STM/STS and DFT calculations, we find that the obtained PbSe−CuSe lateral heterostructure is in weak interaction with the substrate, providing a platform to detect topological properties. Our work expands the strategy of lateral epitaxy of heterostructures based on 2D materials, paving the way toward the production of high-quality monolayers of 2D materials for both fundamental studies and potential applications.

■ EXPERIMENTAL AND CALCULATION DETAILS

Experimental Details. Our experiments were carried out in a home-built ultrahigh vacuum molecular beam epitaxy (UHV-MBE) chamber equipped with an STM (Unisoku). The base pressure of the system is better than 1×10^{-10} Torr. PbSe−CuSe lateral heterostructure was epitaxially grown on Cu(111) substrate by the two-step method in the MBE chamber. Prior to the growth, the Cu(111) substrate was cleaned by several circles of sputtering (800 eV) and annealing (∼850 K, 10 min). Subsequently, Se atoms (99.999%, Alfa Aesar) were thermally evaporated onto the Cu(111) substrate held at room temperature. Then, molecular beam Pb atoms were deposited on the surface. All the STM/STS measurements were conducted at room temperature. The STS (dI/dV−V curve) measurements were acquired by using a standard lock-in technique (793 Hz, 40−50 mV a.c. bias modulation). The system was carefully calibrated by the Si(111)-(7 × 7) and Au(111) surface. The characterization of the sample was also performed with XPS (Kratos Analytical Ltd. AXIS SUPRA with monochromatic 150w Al Kα X-ray).

https://doi.org/10.1021/acsami.2c08397
ACS Appl. Mater. Interfaces 2022, 14, 32738−32746

Calculation Details. First, we used the Device Studio to build the crystal structures involved (Hongzhiwei Technology, Device Studio, Version 2021A, China, 2021. Available online: https://iresearch.net.cn/cloudSoftware). Then, we employed the Vienna ab-initio Simulation Package (VASP)[51] for the first-principles calculations based on DFT. A generalized gradient approximation (GGA) in the form of Perdew−Burke−Ernzerhof functional and HSE06 hybrid functional[52] was adopted for the exchange−correlation functional.[53] The vdW density functional (optB86b-vdW) was capable of treating the dispersion force.[54] The energy convergence value between two consecutive steps was chosen as 10^{-5} eV and maximum force of 0.01 eV/Å was allowed on each atom. The plane-wave basis set with a kinetic energy cutoff of 400 eV was employed. The Cu(111) substrate was simulated by a repeating slab model consisting of a three Cu(111) slab with the calculated lattice constant of 2.56 Å. A 20 Å vacuum slab was considered to avoid the interaction between the supercell with its image. Γ-Centered Monkhorst−Pack mesh was used to sample the Brillouin zone of the supercells.[55] To investigate the bonding situation of the interface, we performed a comprehensive bond analysis using the Lobster package.[56] Lobster allows to project the plane-wave functions to the precious bonding information.

ASSOCIATED CONTENT

Supporting Information

The Supporting Information is available free of charge at https://pubs.acs.org/doi/10.1021/acsami.2c08397.

Atomic resolved STM image of CuSe; schematic of the growth process of the monolayer PbSe; top and side views of the PbSe; simulated STM images of PbSe; Pb adatom adsorption; three typical configurations of CuSe on the Cu(111) substrate; side view of electron localization function; and top view of freestanding PbSe structure, Brillouin zone, and band structures of freestanding PbSe (PDF)

AUTHOR INFORMATION

Corresponding Authors

Ping Li − *State Key Laboratory for Mechanical Behavior of Materials, Center for Spintronics and Quantum Systems, School of Materials Science and Engineering, Xi'an Jiaotong University, Xi'an, Shaanxi 710049, People's Republic of China;* orcid.org/0000-0001-8285-8921; Email: pli@xjtu.edu.cn

Zhihui Qin − *Key Laboratory for Micro/Nano Optoelectronic Devices of Ministry of Education & Hunan Provincial Key Laboratory of Low-Dimensional Structural Physics and Devices, School of Physics and Electronics, Hunan University, Changsha 410082, People's Republic of China;* orcid.org/0000-0003-4145-5741; Email: zhqin@hnu.edu.cn

Lijie Zhang − *Key Laboratory for Micro/Nano Optoelectronic Devices of Ministry of Education & Hunan Provincial Key Laboratory of Low-Dimensional Structural Physics and Devices, School of Physics and Electronics, Hunan University, Changsha 410082, People's Republic of China;* orcid.org/0000-0001-8717-5724; Email: lijiezhang@hnu.edu.cn

Authors

Bo Li − *Key Laboratory for Micro/Nano Optoelectronic Devices of Ministry of Education & Hunan Provincial Key Laboratory of Low-Dimensional Structural Physics and Devices, School of Physics and Electronics, Hunan University, Changsha 410082, People's Republic of China*

Jing Wang − *Key Laboratory for Micro/Nano Optoelectronic Devices of Ministry of Education & Hunan Provincial Key Laboratory of Low-Dimensional Structural Physics and Devices, School of Physics and Electronics, Hunan University, Changsha 410082, People's Republic of China*

Qilong Wu − *Key Laboratory for Micro/Nano Optoelectronic Devices of Ministry of Education & Hunan Provincial Key Laboratory of Low-Dimensional Structural Physics and Devices, School of Physics and Electronics, Hunan University, Changsha 410082, People's Republic of China*

Qiwei Tian − *Key Laboratory for Micro/Nano Optoelectronic Devices of Ministry of Education & Hunan Provincial Key Laboratory of Low-Dimensional Structural Physics and Devices, School of Physics and Electronics, Hunan University, Changsha 410082, People's Republic of China*

Li Zhang − *Key Laboratory for Micro/Nano Optoelectronic Devices of Ministry of Education & Hunan Provincial Key Laboratory of Low-Dimensional Structural Physics and Devices, School of Physics and Electronics, Hunan University, Changsha 410082, People's Republic of China*

Long-Jing Yin − *Key Laboratory for Micro/Nano Optoelectronic Devices of Ministry of Education & Hunan Provincial Key Laboratory of Low-Dimensional Structural Physics and Devices, School of Physics and Electronics, Hunan University, Changsha 410082, People's Republic of China;* orcid.org/0000-0003-1167-5612

Yuan Tian − *Key Laboratory for Micro/Nano Optoelectronic Devices of Ministry of Education & Hunan Provincial Key Laboratory of Low-Dimensional Structural Physics and Devices, School of Physics and Electronics, Hunan University, Changsha 410082, People's Republic of China*

Ping Kwan Johnny Wong − *School of Microelectronics, Northwestern Polytechnical University, Xi'an 710072, People's Republic of China; Shaanxi & NPU Chongqing Technology Innovation Center, Chongqing 400000, People's Republic of China;* orcid.org/0000-0003-4645-0384

Complete contact information is available at: https://pubs.acs.org/10.1021/acsami.2c08397

Notes

The authors declare no competing financial interest.

ACKNOWLEDGMENTS

This work was supported by the National Natural Science Foundation of China (Grant nos. 11904094, 51972106 to L.Z., no. 12174096 to Z.Q., no. 12004295 to P.L., and no. 12174095 to L.-J.Y.), the Strategic Priority Research Program of Chinese Academy of Sciences (Grant no. XDB30000000 to Z.Q.), the Natural Science Foundation of Hunan Province, (Grant No: 2021JJ20026 to L.-J.Y.), the Natural Science Foundation of Shaanxi Province (Grant No: 2021JM-042 to P.K.J. Wong), the Natural Science Foundation of Chongqing, China (Grant No: cstc2021jcyj-msxmX0740 to P.K.J. Wong), and Northwestern Polytechnical University Research Fund for Young Scholars (Grant No. G2022WD01013). The authors also acknowledge the financial support from the Fundamental Research Funds for the Central Universities of China.

REFERENCES

(1) Castro Neto, A. H.; Guinea, F.; Peres, N. M. R.; Novoselov, K. S.; Geim, A. K. The Electronic Properties of Graphene. *Rev. Mod. Phys.* **2009**, *81*, 109.

(2) Feng, B.; Ding, Z.; Meng, S.; Yao, Y.; He, X.; Cheng, P.; Chen, L.; Wu, K. Evidence of Silicene in Honeycomb Structures of Silicon on Ag(111). *Nano Lett.* **2012**, *12*, 3507−3511.

(3) Fleurence, A.; Friedlein, R.; Ozaki, T.; Kawai, H.; Wang, Y.; Yamada-Takamura, Y. Experimental Evidence for Epitaxial Silicene on Diboride Thin Films. *Phys. Rev. Lett.* **2012**, *108*, 245501.

(4) Vogt, P.; De Padova, P.; Quaresima, C.; Avila, J.; Frantzeskakis, E.; Asensio, M. C.; Resta, A.; Ealet, B.; Le Lay, G. Silicene: Compelling Experimental Evidence for Graphenelike Two-Dimensional Silicon. *Phys. Rev. Lett.* **2012**, *108*, 155501.

(5) Chen, L.; Liu, C.-C.; Feng, B.; He, X.; Cheng, P.; Ding, Z.; Meng, S.; Yao, Y.; Wu, K. Evidence for Dirac Fermions in a Honeycomb Lattice Based on Silicon. *Phys. Rev. Lett.* **2012**, *109*, 056804.

(6) Chen, L.; Li, H.; Feng, B.; Ding, Z.; Qiu, J.; Cheng, P.; Wu, K.; Meng, S. Spontaneous Symmetry Breaking and Dynamic Phase Transition in Monolayer Silicene. *Phys. Rev. Lett.* **2013**, *110*, 085504.

(7) Sheng, S.; Wu, J.-b.; Cong, X.; Li, W.; Gou, J.; Zhong, Q.; Cheng, P.; Tan, P.-h.; Chen, L.; Wu, K. Vibrational Properties of a Monolayer Silicene Sheet Studied by Tip-Enhanced Raman Spectroscopy. *Phys. Rev. Lett.* **2017**, *119*, 196803.

(8) Acun, A.; Zhang, L.; Bampoulis, P.; Farmanbar, M.; van Houselt, A.; Rudenko, A. N.; Lingenfelder, M.; Brocks, G.; Poelsema, B.; Katsnelson, M. I.; et al. Germanene: The Germanium Analogue of Graphene. *J. Phys.: Condens. Matter* **2015**, *27*, 443002.

(9) Zhang, L.; Bampoulis, P.; Rudenko, A. N.; Yao, Q.; van Houselt, A.; Poelsema, B.; Katsnelson, M. I.; Zandvliet, H. J. W. Structural and Electronic Properties of Germanene on MoS_2. *Phys. Rev. Lett.* **2016**, *116*, 256804.

(10) Bampoulis, P.; Zhang, L.; Safaei, A.; van Gastel, R.; Poelsema, B.; Zandvliet, H. J. W. Germanene Termination of Ge_2Pt Crystals on Ge(110). *J. Phys.: Condens. Matter* **2014**, *26*, 442001.

(11) Li, L.; Lu, S.-Z.; Pan, J.; Qin, Z.; Wang, Y.-Q.; Wang, Y.; Cao, G.-Y.; Du, S.; Gao, H.-J. Buckled Germanene Formation on Pt(111). *Adv. Mater.* **2014**, *26*, 4820.

(12) Qin, Z.; Pan, J.; Lu, S.; Shao, Y.; Wang, Y.; Du, S.; Gao, H.-J.; Cao, G. Direct Evidence of Dirac Signature in Bilayer Germanene Islands on Cu(111). *Adv. Mater.* **2017**, *29*, 1606046.

(13) Gou, J.; Zhong, Q.; Sheng, S.; Li, W.; Cheng, P.; Li, H.; Chen, L.; Wu, K. Strained Monolayer Germanene with 1 × 1 Lattice on Sb(111). *2D Mater* **2016**, *3*, 045005.

(14) Zhu, F.-F.; Chen, W.-J.; Xu, Y.; Gao, C.-L.; Guan, D.-D.; Liu, C.-H.; Qian, D.; Zhang, S.-C.; Jia, J.-F. Epitaxial Growth of Two-Dimensional Stanene. *Nat. Mater.* **2015**, *14*, 1020−1025.

(15) Deng, J.; Xia, B.; Ma, X.; Chen, H.; Shan, H.; Zhai, X.; Li, B.; Zhao, A.; Xu, Y.; Duan, W.; Zhang, S.-C.; Wang, B.; Hou, J. G. Epitaxial Growth of Ultraflat Stanene with Topological Band Inversion. *Nat. Mater.* **2018**, *17*, 1081−1086.

(16) Gou, J.; Kong, L.; Li, H.; Zhong, Q.; Li, W.; Cheng, P.; Chen, L.; Wu, K. Strain-Induced Band Engineering in Monolayer Stanene on Sb (111). *Phys. Rev. Mater.* **2017**, *1*, 054004.

(17) Reis, F.; Li, G.; Dudy, L.; Bauernfeind, M.; Glass, S.; Hanke, W.; Thomale, R.; Schäfer, J.; Claessen, R. Bismuthene on a Sic Substrate: A Candidate for a High-Temperature Quantum Spin Hall Material. *Science* **2017**, *357*, 287−290.

(18) Kane, C. L.; Mele, E. J. Quantum Spin Hall Effect in Graphene. *Phys. Rev. Lett.* **2005**, *95*, 226801.

(19) Kane, C. L.; Mele, E. J. Z_2 Topological Order and the Quantum Spin Hall Effect. *Phys. Rev. Lett.* **2005**, *95*, 146802.

(20) Liu, C. C.; Feng, W.; Yao, Y. Quantum Spin Hall Effect in Silicene and Two-Dimensional Germanium. *Phys. Rev. Lett.* **2011**, *107*, 076802.

(21) Xu, Y.; Yan, B.; Zhang, H.-J.; Wang, J.; Xu, G.; Tang, P.; Duan, W.; Zhang, S.-C. Large-Gap Quantum Spin Hall Insulators in Tin Films. *Phys. Rev. Lett.* **2013**, *111*, 136804.

(22) Gruznev, D. V.; Eremeev, S. V.; Bondarenko, L. V.; Tupchaya, A. Y.; Yakovlev, A. A.; Mihalyuk, A. N.; Chou, J.-P.; Zotov, A. V.; Saranin, A. A. Two-Dimensional In-Sb Compound on Silicon Hall Insulator. *Nano Lett.* **2018**, *18*, 4338−4345.

(23) Gou, J.; Xia, B.; Li, H.; Wang, X.; Kong, L.; Cheng, P.; Li, H.; Zhang, W.; Qian, T.; Ding, H.; et al. Binary Two-Dimensional Honeycomb Lattice with Strong Spin-Orbit Coupling and Electron-Hole Asymmetry. *Phys. Rev. Lett.* **2018**, *121*, 126801.

(24) Wang, H.; Pei, Y.; LaLonde, A. D.; Snyder, G. J. Heavily Doped P-Type PbSe with High Thermoelectric Performance: An Alternative for PbTe. *Adv. Mater.* **2011**, *23*, 1366−1370.

(25) Jin, S.; Wu, H.; Xu, T. Large Rashba Splitting in Highly Asymmetric CdTe/PbTe/PbSrTe Quantum Well Structures. *Appl. Phys. Lett.* **2009**, *95*, 132105.

(26) Ul Haq, B.; AlFaify, S.; Ahmed, R.; Laref, A.; Mahmood, Q.; Algrafy, E. Optoelectronic Properties of PbSe Monolayers from First-Principles. *Appl. Surf. Sci.* **2020**, *525*, 146521.

(27) Albanesi, E. A.; Okoye, C. M. I.; Rodriguez, C. O.; Peltzer y Blanca, E. L.; Petukhov, A. G. Electronic Structure, Structural Properties, and Dielectric Functions of IV-VI Semiconductors: PbSe and PbTe. *Phys. Rev. B* **2000**, *61*, 16589−16595.

(28) Wrasse, E. O.; Schmidt, T. M. Prediction of Two-Dimensional Topological Crystalline Insulator in PbSe Monolayer. *Nano Lett.* **2014**, *14*, 5717−5720.

(29) Lin, X.; Lu, J. C.; Shao, Y.; Zhang, Y. Y.; Wu, X.; Pan, J. B.; Gao, L.; Zhu, S. Y.; Qian, K.; Zhang, Y. F.; et al. Intrinsically Patterned Two-Dimensional Materials for Selective Adsorption of Molecules and Nanoclusters. *Nat. Mater.* **2017**, *16*, 717−721.

(30) Niu, G.; Lu, J.; Wang, X.; Ruan, Z.; Zhang, H.; Gao, L.; Cai, J.; Lin, X. Se-Concentration Dependent Superstructure Transformations of CuSe Monolayer on Cu(111) Substrate. *2D Mater.* **2021**, *9*, 015017.

(31) Gao, L.; Sun, J. T.; Lu, J. C.; Li, H.; Qian, K.; Zhang, S.; Zhang, Y. Y.; Qian, T.; Ding, H.; Lin, X.; et al. Epitaxial Growth of Honeycomb Monolayer CuSe with Dirac Nodal Line Fermions. *Adv. Mater.* **2018**, *30*, No. e1707055.

(32) Zhu, J.; Liao, X.; Wang, J.; Chen, H.-Y. Photochemical Synthesis and Characterization of PbSe Nanoparticles. *Mater. Res. Bull.* **2001**, *36*, 1169−1176.

(33) Li, X.-B.; Guo, P.; Zhang, Y.-N.; Peng, R.-F.; Zhang, H.; Liu, L.-M. High Carrier Mobility of Few-Layer PbX (X = S, Se, Te). *J. Mater. Chem. C* **2015**, *3*, 6284−6290.

(34) Chang, K.; Kaloni, T. P.; Lin, H.; Bedoya-Pinto, A.; Pandeya, A. K.; Kostanovskiy, I.; Zhao, K.; Zhong, Y.; Hu, X.; Xue, Q. K.; et al. Enhanced Spontaneous Polarization in Ultrathin SnTe Films with Layered Antipolar Structure. *Adv. Mater.* **2019**, *31*, No. e1804428.

(35) Chang, K.; Villanova, J. W. D.; Ji, J. R.; Das, S.; Kuster, F.; Barraza-Lopez, S.; Sessi, P.; Parkin, S. S. P. Vortex-Oriented Ferroelectric Domains in SnTe/PbTe Monolayer Lateral Heterostructures. *Adv. Mater.* **2021**, *33*, No. e2102267.

(36) Shao, Z.; Zheng, F.; Zhang, Z.; Sun, H.; Li, S.; Yuan, H.; Li, Q.; Zhang, P.; Pan, M. Epitaxial Growth of Pbse Few-Layers on $SrTiO_3$: The Effect of Compressive Strain and Potential Two-Dimensional Topological Crystalline Insulator. *ACS Nano* **2019**, *13*, 2615−2623.

(37) Wu, Q.; Fu, X.; Yang, K.; Wu, H.; Liu, L.; Zhang, L.; Tian, Y.; Yin, L.-J.; Huang, W.-Q.; Zhang, W.; et al. Promoting a Weak Coupling of Monolayer $MoSe_2$ Grown on (100)-Faceted Au Foil. *ACS Nano* **2021**, *15*, 4481−4489.

(38) Liu, L.; Park, J.; Siegel, D. A.; McCarty, K. F.; Clark, K. W.; Deng, W.; Basile, L.; Idrobo, J. C.; Li, A.-P.; Gu, G. Heteroepitaxial Growth of Two-Dimensional Hexagonal Boron Nitride Templated by Graphene Edges. *Science* **2014**, *343*, 163−167.

(39) Novoselov, K. S.; Mishchenko, A.; Carvalho, A.; Castro Neto, A. H. 2D Materials and van Der Waals Heterostructures. *Science* **2016**, *353*, aac9439.

(40) Liu, X.; Hersam, M. C. Interface Characterization and Control of 2D Materials and Heterostructures. *Adv. Mater.* **2018**, *30*, No. e1801586.

(41) Hu, J.-P.; He, B.-C.; Wang, H.-B.; Zhang, H.; Huang, C.-Q.; Xie, L.; Guo, X.; Liang, Z.-F.; Chen, S.; Huang, H.; et al. Initial Growth Behavior of Bismuth on Ag(111) and Au(111). *Acta Phys. Sin.* **2022**, *71*, 026101.

(42) Zhou, D.; Li, H.; Si, N.; Jiang, Y.; Huang, H.; Li, H.; Niu, T. Epitaxial Growth of Single Tellurium Atomic Wires on a Cu_2Sb Surface Alloy. *Appl. Phys. Lett.* **2020**, *116*, 061602.

(43) Tian, Q.; He, B.; Zhao, Y.; Wang, S.; Xiao, J.; Song, F.; Wang, Y.; Lu, Y.; Xie, H.; Huang, H.; et al. Electronic Structure Evolution at

https://doi.org/10.1021/acsami.2c08397
ACS Appl. Mater. Interfaces 2022, 14, 32738−32746

DBBA/Au(111) Interface W/O Bismuth Insertion Layer. *Synth. Met.* **2019**, *251*, 24−29.
(44) He, B.; Tian, G.; Gou, J.; Liu, B.; Shen, K.; Tian, Q.; Yu, Z.; Song, F.; Xie, H.; Gao, Y.; et al. Structural and Electronic Properties of Atomically Thin Bismuth on Au(111). *Surf. Sci.* **2019**, *679*, 147−153.
(45) Sahoo, P. K.; Memaran, S.; Xin, Y.; Balicas, L.; Gutiérrez, H. R. One-Pot Growth of Two-Dimensional Lateral Heterostructures via Sequential Edge-Epitaxy. *Nature* **2018**, *553*, 63−67.
(46) Levendorf, M. P.; Kim, C.-J.; Brown, L.; Huang, P. Y.; Havener, R. W.; Muller, D. A.; Park, J. Graphene and Boron Nitride Lateral Heterostructures for Atomically Thin Circuitry. *Nature* **2012**, *488*, 627−632.
(47) Liu, X.; Hersam, M. C. Borophene-Graphene Heterostructures. *Sci. Adv.* **2019**, *5*, No. eaax6444.
(48) Ruan, Q.; Wang, L.; Bets, K. V.; Yakobson, B. I. Step-Edge Epitaxy for Borophene Growth on Insulators. *ACS Nano* **2021**, *15*, 18347−18353.
(49) Li, P.; Zhou, X.-S.; Guo, Z.-X. Intriguing Magnetoelectric Effect in Two-Dimensional Ferromagnetic/Perovskite Oxide Ferroelectric Heterostructure. *npj Comput. Mater.* **2022**, *8*, 20.
(50) Kastner, M.; Adler, D.; Fritzsche, H. Valence-Alternation Model for Localized Gap States in Lone-Pair Semiconductors. *Phys. Rev. Lett.* **1976**, *37*, 1504.
(51) Kresse, G.; Furthmüller, J. Efficient Iterative Schemes for Ab Initio Total-Energy Calculations Using a Plane-Wave Basis Set. *Phys. Rev. B* **1996**, *54*, 11169.
(52) Heyd, J.; Scuseria, G. E.; Ernzerhof, M. Hybrid Functionals Based on a Screened Coulomb Potential. *J. Chem. Phys.* **2003**, *118*, 8207−8215.
(53) Perdew, J. P.; Burke, K.; Ernzerhof, M. Generalized Gradient Approximation Made Simple. *Phys. Rev. Lett.* **1996**, *77*, 3865.
(54) Dion, M.; Rydberg, H.; Schröder, E.; Langreth, D. C.; Lundqvist, B. I. Van Der Waals Density Functional for General Geometries. *Phys. Rev. Lett.* **2004**, *92*, 246401.
(55) Monkhorst, H. J.; Pack, J. D. Special Points for Brillouin-Zone Integrations. *Phys. Rev. B* **1976**, *13*, 5188.
(56) Maintz, S.; Deringer, V. L.; Tchougréeff, A. L.; Dronskowski, R. Lobster: A Tool to Extract Chemical Bonding from Plane-Wave Based DFT. *J. Comput. Chem.* **2016**, *37*, 1030−1035.